Available online at www.eccomasproceedia.org
Eccomas Proceedia COMPDYN (2025) 1119-1127

ECCOMAS Proceedia

COMPDYN 2025
10th ECCOMAS Thematic Conference on
Computational Methods in Structural Dynamics and Earthquake Engineering
M. Papadrakakis, M. Fragiadakis (eds.)
Rhodes Island, Greece, 15-18 June 2025

WAVE PROPAGATION AND COMPLETE BAND GAP FORMATION IN MIURA-ORI METABEAMS

Elisabetta Manconi[1,*], Marco Riboli[2], Alessandro Contini [1], Luca Collini [1]

[1]Department of Industrial Engineering Systems and Technologies
University of Parma, Italy
e-mail: elisabetta.manconi@unipr.it

[2] Department of Innovative Technologies
University of Applied Sciences of Southern Switzerland, SUPSI, Lugano, Switzerland

Abstract. *Periodic structures with complete band gap formation can provide excellent vibroacoustic isolation and protection. In this context, origami-inspired periodic designs have demonstrated outstanding properties, making them highly effective for a variety of static and dynamic applications. In particular, Miura origami has attracted interest in metamaterials research due to its simple, foldable, and reconfigurable nature. This work aims to investigate wave propagation and band gap formation in origami-inspired structures, focusing on the first band gap formation in Miura-ori beams. The study presents a Wave and Finite Element approach for systematically predicting dispersion curves and band gaps under parametric variations of the Miura-ori unit cell geometry. The dispersion curves are presented and discussed, illustrating the effects of the folding angle on the prediction of the first complete band gaps, where wave propagation is prohibited in all directions. The effectiveness of the Miura-ori metabeam in attenuating vibration transmission is evaluated quantitatively, and the structure's deformation under the passage of harmonic disturbances is depicted graphically and using energy parameters.*

Keywords: Miura origami, metamaterials, band gap, wave propagation, vibration isolation. metabarriers

Peer-review under responsibility of the organizing committee of COMPDYN 2025.
doi: 10.7712/120125.12476.25081

1 INTRODUCTION

Mechanical metamaterials can be seen as artificial materials whose mechanical properties are primarily defined by their structural arrangement rather than their constituent material properties. Among these, origami-based metamaterials are particularly promising since their folding principles can introduce structural reconfigurability, lightweightness, and enhanced control over dynamic responses. For example, Thota and Wang [1] have demonstrated that by attaching cylindrical inclusions on top of a foldable origami sheet, the resulting periodic lattice can be reconfigured through folding to enable tunable waveguiding capabilities and transformation between different Bravais-lattice types with minimal actuation effort.

Miura-ori structures are notable in origami-inspired metamaterials due to their simple foldable nature and distinctive geometric features [2]. These structures consist of periodic parallelogram facets that can be compressed or expanded with relative ease, thus enabling potential tunability of their vibrational and acoustic performance. Miura-ori structures can be deployed, exploiting their rigid kinematics, or morphed by deforming the facets, for example using a distributed network of actuators, e.g., [3]. This suggests the possibility of dynamically changing not only the mechanical properties of the structure but also its phononic characteristics. Moreover, recent studies have further extended the potential of Miura-ori structures by modifying their design, as in [4] where a novel perforated Miura-ori phononic structure (PMPS) capable of tuning complete and partial band gaps through folding was investigated.

This work deals with the study of wave propagation and band gap formation in origami waveguides. We consider a Miura-ori beam composed of a single strip of Miura-ori unit cells repeated along the wave propagation direction, and we apply a Wave and Finite Element approach (WFE), [5–7], to systematically predict dispersion curves and band gaps under the parametric variation of the geometry of the Miura-ori unit cell. This combined wave-based and finite element approach can accurately capture the dispersion behaviour and band gap formation across a wide frequency spectrum using a 3D solid elements mesh at low computational cost, providing an accurate representation of the folding-induced geometrical complexity.

The main contributions of this work can be summarised as follows:

- the influence of geometric modifications in the Miura-ori unit cell on the first band gap is investigated, offering insights into potential design and tuning strategies;
- the efficiency of Miura-ori beams in attenuating vibrational transmission by the formation of a first complete band gap is quantitatively assessed, highlighting their effectiveness for vibration isolation;
- the structure's deformation and energy distribution under harmonic excitations are presented in terms of wave-modes representation and energy flow evaluation.

The remainder of the paper is organised as follows. Section 2 introduces the geometric parameters of the Miura-ori unit-cell and its WFE model. In Section 3 a numerical example is presented to show wave characterisation in terms of dispersion curves, wavemodes, and energy related quantities. The formation of the first complete stop band is discussed and the effect of the folding angle is presented. Concluding remarks are finally given in Section 4.

2 WAVE FINITE ELEMENT MODELLING OF THE MIURA-ORI WAVEGUIDE

This research examines a Miura-ori beam, which is created through the repeated arrangement of Miura-ori unit cells in one direction. As illustrated in Figure 1, each unit cell is defined by parallelogram faces with side lengths a and b and an acute angle $\beta \in [0^\circ, 90^\circ]$. The configuration of the beam is characterised by the folding angle $\phi \in [0^\circ, 2\beta]$, which governs the degree of

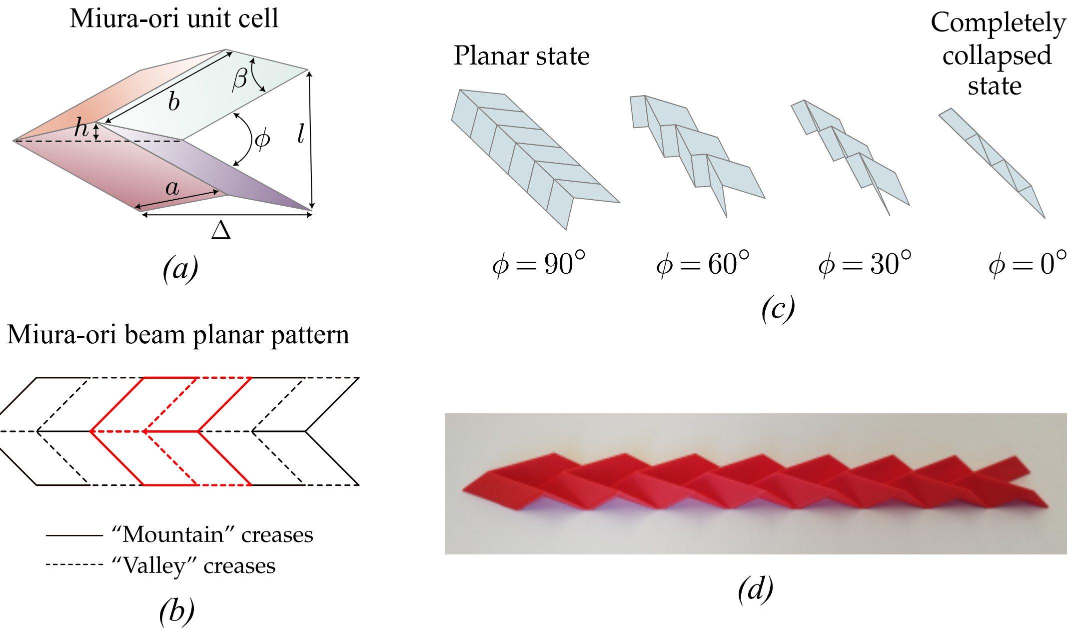

Figure 1: Miura-ori beam. Specifically for this illustration, $\beta = 45°$, $a/b = 1/\sqrt{2}$ (a) Unitary cell. (b) Planar pattern of a Miura-ori strip. (c) Different fold configurations of a Miura-ori strip. (d) Photo of a real 3D-printed Miura-ori beam ($\phi = 45°$).

compaction of the structure: $\phi = 2\beta$ corresponds to the fully planar state, whereas $\phi = 0°$ represents the completely collapsed configuration.

The dimensions of the unit cell along the principal directions are given by:

$$l = 2b\sin\left(\frac{\phi}{2}\right), \Delta = 2a\frac{\cos\beta}{\cos\left(\frac{\phi}{2}\right)}, h = a\frac{\sqrt{\sin^2\beta - \sin^2\left(\frac{\phi}{2}\right)}}{\cos\left(\frac{\phi}{2}\right)}. \tag{1}$$

The repetition of these unit cells along a defined direction forms a Miura-ori beam, whose geometry and mechanical response can be adjusted by varying the parameters a, b, β, and ϕ.

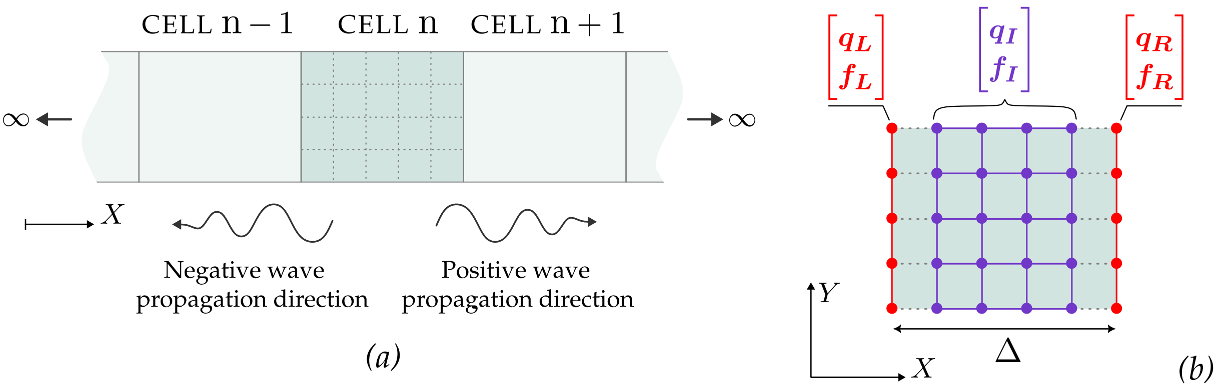

Figure 2: (a) 1D periodic waveguide. (b) FE model of the unit cell.

Figure 2a shows a periodic 1D waveguide, where wave propagation is in the X-direction. In Figure 2b a unit cell is described by a Finite Element model with N degrees of freedom (DoF).

Here Δ is the period (length of the unit cell, or periodic length). The FE model comprises a set of boundary state variables referred to as external $\boldsymbol{E}$ - located to the left and right of the unit cell - and a set of internal states $\boldsymbol{I}$. Assuming $\boldsymbol{f_I} = \boldsymbol{0}$ and no damping, the dynamics of the unit cell can be represented by the equation of motion

$$\underbrace{\left(\boldsymbol{K} - \omega^2 \boldsymbol{M}\right)}_{\boldsymbol{D}(\omega)} \boldsymbol{q} = \boldsymbol{f} \;\Rightarrow\; \begin{array}{r c c} & \mathrm{N}_E \text{ col.s} & \mathrm{N}_I \text{ col.s} \\ \mathrm{N}_E \text{ rows} \rightarrow & \multicolumn{2}{c}{\begin{bmatrix} \boldsymbol{D_{EE}}(\omega) & \boldsymbol{D_{EI}}(\omega) \\ \boldsymbol{D_{IE}}(\omega) & \boldsymbol{D_{II}}(\omega) \end{bmatrix}} \\ \mathrm{N}_I \text{ rows} \rightarrow & & \end{array} \begin{bmatrix} \boldsymbol{q_E} \\ \boldsymbol{q_I} \end{bmatrix} = \begin{bmatrix} \boldsymbol{f_E} \\ \boldsymbol{0} \end{bmatrix}, \tag{2}$$

where $\boldsymbol{D}(\omega) : \mathbb{R} \rightarrow \mathbb{R}^{\mathrm{N}\times\mathrm{N}}$ is the dynamic stiffness matrix while $\boldsymbol{q}$ and $\boldsymbol{f}$ typically are nodal displacements and forces. According to this notation, N_E refers to the number of external DoF, and N_I to the internal DoF, with $\mathrm{N} = \mathrm{N}_E + \mathrm{N}_I$.

Left and right boundary states are related by periodicity conditions while internal states are dynamically condensed. After condensation of the internal states, a reduced dynamic stiffness matrix is obtained as $\widetilde{\boldsymbol{D}}\,(\omega) = \boldsymbol{R}^T \boldsymbol{D}(\omega) \boldsymbol{R}$, where

$$\boldsymbol{R} = \begin{bmatrix} \boldsymbol{I} \\ -\left[\boldsymbol{D_{II}}(\omega)\right]^{-1} \boldsymbol{D_{IE}}(\omega) \end{bmatrix}.$$

It follows the reduced system:

$$\widetilde{\boldsymbol{D}}\,(\omega) \boldsymbol{q_E} = \boldsymbol{f_E} \;\Rightarrow\; \begin{bmatrix} \widetilde{\boldsymbol{D}}_{\boldsymbol{LL}}\,(\omega) & \widetilde{\boldsymbol{D}}_{\boldsymbol{LR}}\,(\omega) \\ \widetilde{\boldsymbol{D}}_{\boldsymbol{RL}}\,(\omega) & \widetilde{\boldsymbol{D}}_{\boldsymbol{RR}}\,(\omega) \end{bmatrix} \begin{bmatrix} \boldsymbol{q_L} \\ \boldsymbol{q_R} \end{bmatrix} = \begin{bmatrix} \boldsymbol{f_L} \\ \boldsymbol{f_R} \end{bmatrix},$$

where the subscripts $\boldsymbol{L}$ and $\boldsymbol{R}$ denote the left and right boundaries of the unit cell. Finally, by applying the periodicity conditions, the following quadratic eigenvalue problem (QEP) in the complex variable λ can be formulated:

$$\begin{cases} \left(\boldsymbol{\Lambda}^{*T}\, \widetilde{\boldsymbol{D}}\,(\omega) \boldsymbol{\Lambda}\right) \boldsymbol{q_L} = \boldsymbol{0}, \\ \boldsymbol{\Lambda} = \begin{bmatrix} \boldsymbol{I} & \lambda \boldsymbol{I} \end{bmatrix}^T, \end{cases} \tag{3}$$

where * we refer to the conjugate. The problem (3) can be solved using standard methods for a specific value of ω, yielding the eigenvalues λ_j and the corresponding eigenvectors $\boldsymbol{\nu_j}$, with $j = 1, \ldots, \mathrm{N}_E$. The eigenvectors describe the wave shapes. In general, the eigenpairs $\{\lambda_j, \boldsymbol{\nu_j}\}$ can be used to transform the problem into the wave domain.

According to the Floquet theorem [8], the state variables at the left and right boundaries of a cell are related by

$$\begin{cases} \begin{bmatrix} \boldsymbol{q_R} \\ \boldsymbol{f_R} \end{bmatrix} = \lambda_j \begin{bmatrix} \boldsymbol{q_L} \\ \boldsymbol{f_L} \end{bmatrix} \\ \lambda_j = e^{-i\mu_j} \end{cases}, \tag{4}$$

where $i = \sqrt{-1}$ is the imaginary unit and μ_j is the propagation constant. A purely real propagation constant indicates a wave that propagates and efficiently transmits energy through the structure, a purely imaginary propagation constant corresponds to an evanescent wave that decays in space, while a complex propagation constant corresponds to an attenuating wave. The following energy related quantities are introduced [5]:

$$v_e = \frac{\frac{\omega}{2} Im(\mathbf{F}_L^* \mathbf{q}_L)}{\langle E \rangle / \Delta}, \tag{5}$$

is the energy velocity given by the ratio of the time average energy flow and the time average energy density;

$$\langle E\rangle = \langle E_k\rangle + \langle E_p\rangle = \frac{\omega^2}{4} Re\left[\mathbf{V}_j^{*}\mathbf{M}\mathbf{V}_j\right] + \frac{1}{4} Re\left[\mathbf{V}_j^{*}\mathbf{K}\mathbf{V}_j\right] \tag{6}$$

is the time average total energy stored in the segment, given by the sum of $\langle E_k\rangle$ time average kinetic energy and the $\langle E_p\rangle$ potential energy.

3 NUMERICAL EXAMPLE

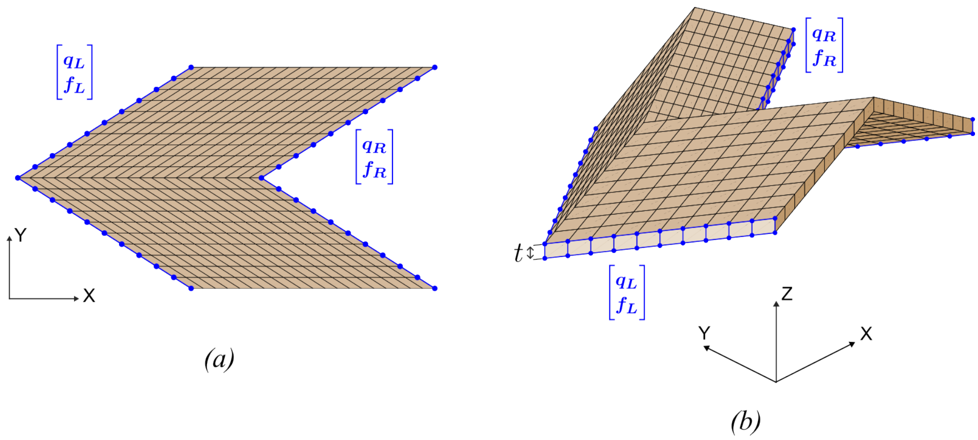

Figure 3: Miura-ori unit cell FEM model. (a) Top view. (b) Axonometric view.

In this section, the method presented in Section 2 is applied to predict the dispersion curves and wavemodes of a Miura-ori metabeam as described in Figure 1, where $\Phi = \pi/4$, $\beta = \pi/4$, $b/a = \sqrt{2}$ and $a/t = 40$, where t is the facet thickness. Material considered for this case is aluminium.

The FE model for this system is realised using five 3D solid structural brick elements for each facet, similarly to the model depicted in Figure 3. The elements used are of the type Solid45 in Ansys - eight nodes and three degrees of freedom per node: u_x, u_y and u_z. The dimensionless frequency $\Omega = \frac{\omega\Delta}{c_L}$ is introduced to present the results, where $c_L = \sqrt{\frac{E}{\rho}}$ is the propagation velocity of longitudinal waves in the material.

Figure 4 shows the dispersion curves for free waves propagating in the positive X direction.

Label	E_x/E_{tot} (%)	E_y/E_{tot} (%)	E_z/E_{tot} (%)	v_e (m/s)
A	60.8311	35.4117	3.7572	0.0058
B	14.3241	31.2778	54.3981	0.0030
C	1.4928	56.0897	42.4175	0.0002
D	7.1235	87.7070	5.1695	0.0004

Table 1: Percentage of the kinetic energy in the X, Y and Z directions and energy velocity (5) for selected wavemodes as in Figure 4.

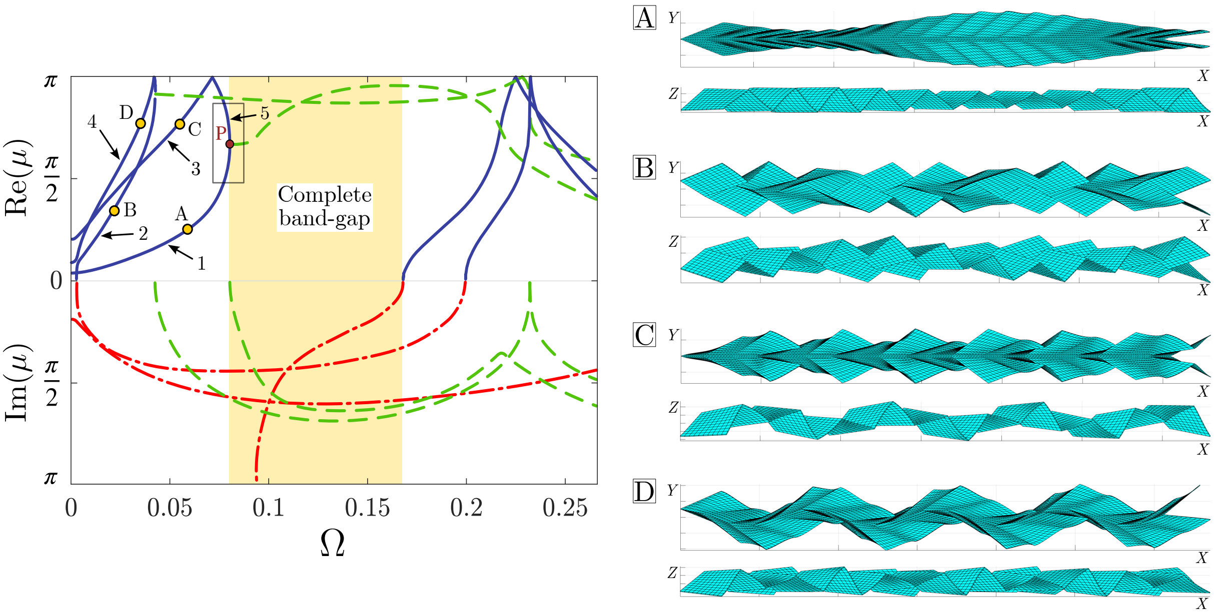

Figure 4: Complex dispersion curves for wave propagating in the positive X direction and wavemodes. Blue solid lines: pure propagating waves; dash-dot red lines: evanescent waves; dashed green lines: attenuating waves.

The yellow area in Figure 4 represents the first complete stop band. It can be seen that no branches corresponding to propagating waves (depicted in the figure by the blue lines) exist in this area, indicating that all possible wave modes in the 3D model of the structure cannot propagate and that vibrational energy cannot be transmitted.

Although it is common at low frequencies to describe the wave modes in terms of fundamental transverse, extensional, and shear waves in a beam, Figure 4 shows that the wave behaviour starts to become complicated at low frequencies due to the folding. To understand the nature of wave propagation, the wave modes at selected frequencies can be represented graphically. These are shown in Figure 4 for different points, illustrating the metabeam displacements in the $Y-X$ and $Z-X$ planes under the passage of a pure harmonic disturbance. Table 1 displays the percentage of kinetic energy in the X, Y, and Z directions for the same points, where the total time-averaged energy density in the unit cell is evaluated using Equation (6). As an example, branch 1 exhibits predominantly extensional deformation (for point A, the main energy contribution is in the X direction $\langle E_x \rangle / \langle E \rangle = 60.8$ with significant transverse displacements due to the striction effects $\langle E_y \rangle / \langle E \rangle = 35.4$), branch 2 show a shear behaviour ($\langle E_z \rangle / \langle E \rangle = 54.4$, $\langle E_y \rangle / \langle E \rangle = 31.3$), branch 3 a flexural ($\langle E_y \rangle / \langle E \rangle = 87.7$), etc. For each point, the energy velocity is presented as an important parameter to predict contradirectional coupling (locking), as described in [9]. These couplings give rise to the band gap indicated in yellow in Figure 4.

Figure 5 and Table 2 illustrate the evolution of wavemodes near the coupling point P, which occurs at $\Omega \simeq 0.08$. In the vicinity of P, the two real branches 1 and 5 (propagating waves) have opposite energy velocities. The results indicate that, as the frequency increases, the wave modes represented by branches 1 and 5 change rapidly, as seen at points E, F and G, H, until they become similar, as at I and J, merging and ultimately becoming complex.

An effective way to illustrate stop bands is to plot $|\lambda|$ against frequency, resulting in characteristic "bubbles" around unity. The horizontal span of each bubble indicates the bandwidth of the stop band, while its vertical extent reflects the attenuation level. At the frequency ω, the j^{th} harmonic wave propagates freely when μ_j is purely real, meaning that the absolute value of $|\lambda_j|$

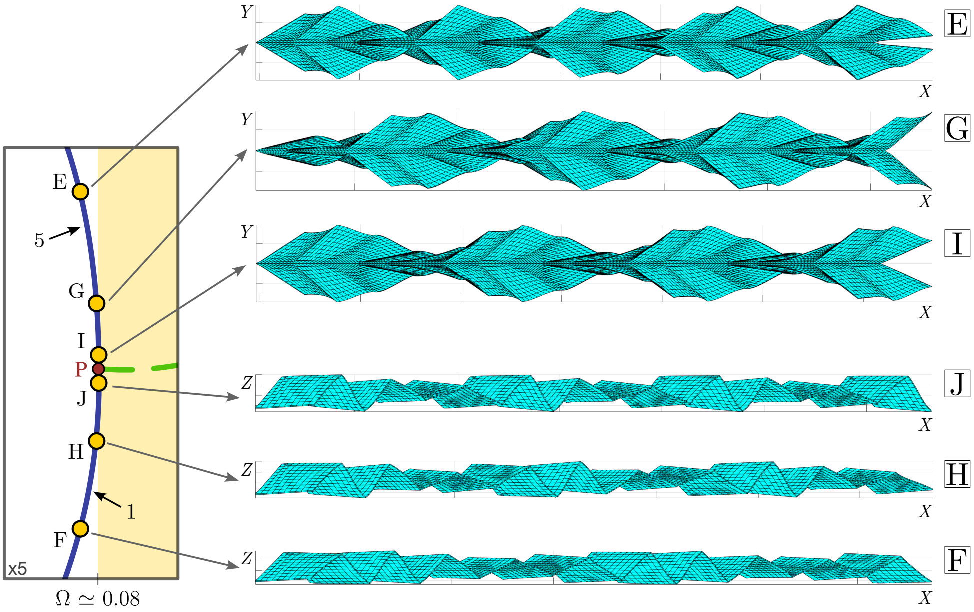

Figure 5: Complex dispersion curves and wavemodes in the vicinity of point P in Figure 4. Blue solid lines: pure propagating waves; dash-dot red lines: evanescent waves; dashed green lines: attenuating waves.

Label	E_x/E_{tot} (%)	E_y/E_{tot} (%)	E_z/E_{tot} (%)	v_e (m/s)
E	20.9541	52.4521	26.5938	-0.0019
F	39.7584	52.7002	7.5414	0.0026
G	25.0626	57.4943	17.4431	-0.0006
H	30.0734	57.9569	11.9697	0.0007
I	26.9321	58.1719	14.8960	-0.000095
J	27.6785	58.2479	14.0736	0.000096

Table 2: Percentage of the kinetic energy in the X, Y and Z directions and energy velocity (5) for selected wavemodes as in Figure 5.

equals one. When μ_j is complex and $|\lambda_j| \neq 1$, harmonic waves cannot propagate. Thus, pass and stop bands can be identified when $|\lambda_j| = 1$ and $\lambda_j \neq 1$ respectively.

Figure 6(a) shows the absolute value of λ with respect to Ω for $\phi = 45°$, clearly demonstrating the formation of the first complete band gap, which corresponds to those shown in Figure 4. It is evident that the starting frequency of the second bubble, relating to the first quasi-extensional wave modes, coincides with the lower bounding frequency of the first complete band gap. Figure 6(b) shows how the first complete stop band changes with different folding angles (ϕ). It can be seen that the first complete stop band widens as the folding angle increases while its starting frequency increases slightly.

4 CONCLUSIONS

In this work wave propagation and complete band gap formation in Miura-ori metabeams were studied using a Wave and Finite Element (WFE) method. The method was applied considering a Miura-ori unit cell discretised using 3D brick elements. The results showed that the

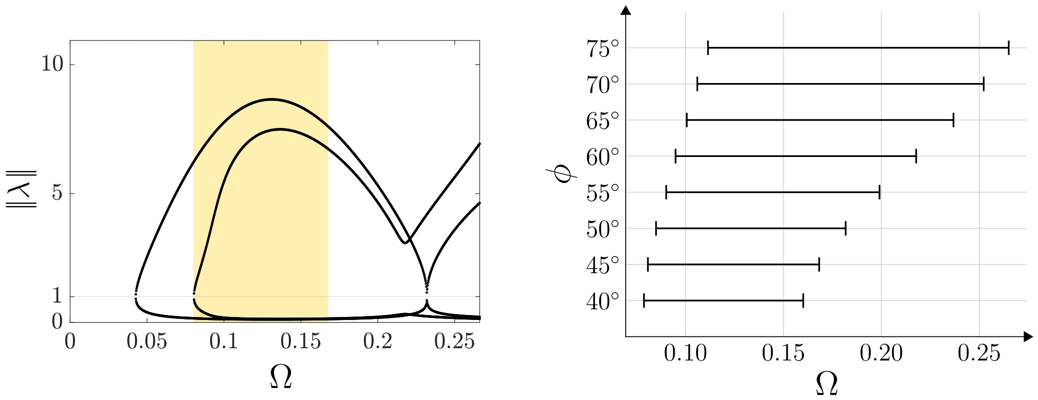

(a) *(b)*

Figure 6: Band gaps of the Miura-Ori metabeam. (a) Band gaps corresponding to the case presented in Figure 4; (b) First complete band gap for different values of the folding angle ϕ.

formation of a complete band gap occurs at the frequency where the propagating waves couple. Dispersion curves and wave mode analyses highlighted the role of contradirectional wave coupling in the formation of this complete band gap. It was shown that the geometric parameters, particularly the folding angle, significantly influence the width of the first complete stop band. These findings underline the potential of Miura-ori metabeams as tunable solutions for vibration isolation and wave filtering applications.

Acknowledgements. Part of this work was carried out while the first author was a posdoctoral fellow at the University Parma, Italy. Research supported by PNRR MISSION 4 COMPONENT 2 INVESTMENT 1.3 – Funded by NEXTGENERATION EU – Research program PE00000004 “Made in Italy Circolare e Sostenibile - MICS” funded by DD n.1551, 11.10.2022 on PNRR MUR – M4C2 – Investment 1.3 –”Partenariati estesi alle università, ai centri di ricerca, alle aziende per il finanziamento di progetti di ricerca di base” - D.D. n. 341, 15 marzo 2022. CUP D43C22003120001

References

[1] M. Thota, K. Wang, Tunable waveguiding in origami phononic structures, Journal of Sound and Vibration 430 (2018) 93–100. `doi:https://doi.org/10.1016/j.jsv.2018.05.031`.

[2] P. Yan, H. Huang, M. Meloni, B. Li, J. Cai, Mechanical properties inside origami-inspired structures: An overview, Applied Mechanics Reviews 77 (2024) 1–129. `doi:10.1115/1.4066566`.

[3] S. W. Grey, F. Scarpa, M. Schenk, Embedded actuation for shape-adaptive origami, Journal of Mechanical Design 143 (8) (2021) 081703. `doi:10.1115/1.4049880`.

[4] X. Zhang, X. Huang, G. Lu, Tunable bandgaps and acoustic characteristics of perforated miura-ori phononic structures, International Journal of Mechanical Sciences 253 (2023) 108389. `doi:https://doi.org/10.1016/j.ijmecsci.2023.108389`.

[5] B. Mace, D. Duhamel, M. Brennan, L. Hinke, Finite element prediction of wave motion

in structural waveguides, The Journal of the Acoustical Society of America 117 (2005) 2835–43. doi:10.1121/1.1887126.

[6] B. Mace, E. Manconi, Modelling wave propagation in two-dimensional structures using finite element analysis, Journal of Sound and Vibration 318 (2008) 884–902. doi:10.1016/j.jsv.2008.04.039.

[7] J. Renno, E. Manconi, B. Mace, A finite element method for modelling waves in laminated structures, Advances in Structural Engineering 16 (2013) 61–76. doi:10.1260/1369-4332.16.1.61.

[8] G. Floquet, Sur les équations différentielles linéaires à coefficients périodiques, Annales scientifiques de l'École Normale Supérieure 2e série, 12 (1883) 47–88. doi:10.24033/asens.220.

[9] M. E. Mace BR, Wave motion and dispersion phenomena: veering, locking and strong coupling effects, J Acoust Soc Am. 229 (2012) 1015–1028. doi:10.1121/1.3672647.